ChemElectroChem

Research Article
doi.org/10.1002/celc.202200859

Chemistry Europe
European Chemical Societies Publishing

www.chemelectrochem.org

A Single-Pot Co-Precipitation Synthesis Route for Ni-Rich Layered Oxide Materials with High Cycling Stability

Harald Norrud Pollen,[a] Julian Richard Tolchard,[b] Ann Mari Svensson,[a] and Nils Peter Wagner*[a, b]

In this work we report variations of $LiNi_{0.88}Mn_{0.06}Co_{0.06}O_2$ synthesised through a single-pot oxalic acid co-precipitation route, in which all cation precursors were added in the same step. The effects of Al-doping, heat-treatment temperature and Li precursor excess were investigated with physicochemical and electrochemical characterisation. Phase pure and well-ordered polycrystalline materials were successfully synthesised for all Al-doped and undoped compositions. Undoped $LiNi_{0.88}Mn_{0.06}Co_{0.06}O_2$ prepared at 750 °C with 4 at% excess Li precursor showed excellent cycling stability in NMC||LTO cells with an initial capacity of 201 mAh/g at 0.1 C at 20 °C, and a capacity retention of 81% after 415 cycles. The Al-doped variations $LiNi_{0.88}Mn_{0.04}Co_{0.06}Al_{0.02}O_2$ and $LiNi_{0.88}Mn_{0.06}Co_{0.04}Al_{0.02}O_2$ were synthesised, and they showed similar initial electrochemical performance to undoped $LiNi_{0.88}Mn_{0.06}Co_{0.06}O_2$, but Al-doping via the oxalic acid co-precipitation route resulted in shorter cycle life. The study outlines the importance of the processing parameters to achieve Ni-rich layered oxides with a long cycle life without further surface modifications.

Introduction

Li-ion batteries have a central role in enabling the transition to renewable energy sources, particularly within the transportation sector where high energy densities are essential for electric vehicles with long range. Ni-rich layered oxides ($LiNi_xM_{1-x}O_2$, $x > 0.5$) are the current default choice for high-energy cathode materials for Li-ion batteries, and combine a high capacity of over 200 mAh/g at the active material level with a high voltage of ~4 V vs Li/Li^+.[1,2] A push towards higher Ni-content within these is fuelled by a corresponding increase in capacity, with concurrent cost- and ethical-benefits from lowering the Co-content. However, the cycle life and the thermal stability also decrease with increasing content of Ni.[3–6]

$LiNi_xMn_yCo_zO_2$ (NMC) and $LiNi_xCo_yAl_zO_2$ (NCA) are two of the main compositional subclasses within Ni-rich layered oxides, and are reported to be commercially available at 80 at% Ni.[7–9] These materials are isostructural to $LiCoO_2$ (LCO) and can be described as having a rock-salt-derived structure consisting of edge-sharing octahedra ordered in alternating layers of TMO_6 and LiO_6.[10–14] This allows for 2D diffusion of Li^+ within the LiO_6 layers. However, Ni-rich layered oxides are not perfectly ordered, as the proximate ionic radii of Li^+ and Ni^{2+} ($r(Li^+) = 76$ pm and $r(Ni^{2+}) = 69$ pm[15]) allow for anti-site disorder (or cation mixing) to occur,[16–18] which can impede Li^+ diffusion.[19,20] One of the main capacity fading mechanisms for Ni-rich layered oxides with respect to cycle life is a surface reconstruction, where the layered structure transforms into a spinel-like phase and a rock-salt phase at the delithiated surface,[18,21,22] clogging the Li^+ diffusion channels. These phase transitions can be attributed to unstable Ni^{4+} present at high levels of delithiation, which can be reduced to Ni^{2+} and enter the Li-layer. Such surface reconstruction is also associated with an oxygen release from the lattice to charge-compensate for the Ni^{4+} to Ni^{2+} reduction.[22–24] The anisotropic volume change associated with Li^+ removal and insertion is another challenge. During delithiation the layered oxides with high Ni-content go through a series of phase transitions between hexagonal and monoclinic phases. The layered structure collapses along the c-axis at a highly delithiated state associated with a transition between two hexagonal phases, commonly denoted H2 and H3.[25–28] The volume changes accompanying the phase transitions can induce contact loss between particles and microcracks when repeated upon cycling.[6,18,27,29] Electrolyte can infiltrate the core of the particles via the microcracks, exposing new surfaces to the electrolyte and triggering further surface reconstruction and parasitic reactions.[6,27] Ni-rich layered oxides are also known to be air sensitive as they react with CO_2 and H_2O forming residual Li compounds, such as LiOH and Li_2CO_3,[24,30] if stored incorrectly. These surface residual compounds can be detrimental for the electrochemical performance.[31–33]

The various metal elements serve different purposes in NMC. A higher Ni-content is linked to a higher capacity as it is the main electrochemically active element. Mn is electrochemically inactive but contributes to the structural stability. Co

[a] H. N. Pollen, Prof. A. M. Svensson, Assoc. Prof. N. P. Wagner
Department of Materials Science and Engineering
NTNU Norwegian University of Science and Technology
7491 Trondheim, Norway
E-mail: nils.p.wagner@ntnu.no
[b] Dr. J. R. Tolchard, Assoc. Prof. N. P. Wagner
Department of Sustainable Energy Technology
SINTEF Industry
7491 Trondheim, Norway

Supporting information for this article is available on the WWW under https://doi.org/10.1002/celc.202200859

contributes to both a well-ordered structure and improved rate capabilities.[3,34,35] Several studies have observed that incorporating Al^{3+} in NMC to form NMCA has improved the cycle life,[36–38] and Al^{3+} has been reported to suppress the H2-H3 phase transition associated anisotropic volume change.[39,40] Nb^{5+} and Mg^{2+} are other doping elements that have been explored to counteract the instability issues of Ni-rich NMC.[41–43] As the Ni-content increases there is correspondingly less substitutional freedom, and which supporting elements to include should be carefully considered due to their differing properties.

Hydroxide co-precipitation is a typical synthesis route to obtain Ni-rich layered oxides. In this route, a stoichiometric ratio of Ni^{2+}, Mn^{2+} and Co^{2+} is precipitated as hydroxide compounds ($M(OH)_2$) in an alkaline environment. Afterwards a Li precursor (LiOH or Li_2CO_3) and (if applicable) an Al precursor ($Al(OH)_3$) are added, mixed and reacted by a solid-state mechanism at a high temperature in an oxidative environment, to form the lithiated layered structure.[38,44,45] The Li precursor is added in an excess amount to compensate for its volatility during the high temperature heat-treatment.[44,46,47] Earlier studies have shown that the heat-treatment temperature and holding time can affect the structural quality, particle morphology and the electrochemical properties.[44,48–51] Ni-rich layered oxides are considered difficult to synthesise as they are sensitive to stoichiometric offsets: $Li_{1-z}Ni_{1+z}O_2$ can be formed in a Li-deficient material, where excessive Ni enters the Li-layer as Ni^{2+}.[17,46] However, too much Li precursor can also form undesirable amounts of residual Li compounds on the surface.[47,49,52] The combination of heat-treatment process parameters and amount of Li precursor should be carefully balanced to achieve a well-ordered structure with a low degree of cation mixing and low amounts of surface impurities.

In this work variations of $LiNi_{0.88}Mn_{0.06}Co_{0.06}O_2$ are synthesised through a single-pot oxalic co-precipitation route, in which the oxalic acid serves as the precipitation agent. Compositional differences by Al-doping, and the process parameters heat-treatment temperature and amount of excess Li precursor are investigated. The single-pot co-precipitation in this work takes place in an acidic environment, allowing all the cation components to be included simultaneously by co-precipitation, including Li and Al, with the aim to distribute Li and Al precursors uniformly amongst the precipitated particles before the heat-treatment. Al-doped variations are prepared by substituting either Mn or Co with 2 at% Al, as minor compositional differences may prove important at a high Ni-content. The studied compositions are $LiNi_{0.88}Mn_{0.06}Co_{0.06}O_2$ (NMC), $LiNi_{0.88}Mn_{0.04}Co_{0.06}Al_{0.02}O_2$ (NMCA–Mn) and $LiNi_{0.88}Mn_{0.06}Co_{0.04}Al_{0.02}O_2$ (NMCA–Co). Heat-treatment temperatures in the range 750–850 °C are explored, along with lithium precursor excess in the range 4–15 at%, as these synthesis parameters are considered to be important to the crystal structure and the particle morphology. Synthesised materials are characterised physicochemically to evaluate composition, structure, and morphology. Electrochemical properties are evaluated through cycling tests, rate tests and electrochemical impedance spectroscopy.

The first part of this work explores different compositional variations of Al-doped and undoped $LiNi_{0.88}Mn_{0.06}Co_{0.06}O_2$ prepared at different heat-treatment temperatures, with a fixed amount of excess Li precursor of 7.5 at%. Afterwards, the best performing combination of composition and temperature is fixed and the effect of excess Li precursor is studied.

Results and Discussion

Part A: Determining the composition and heat-treatment temperature

The transition metal ratio of the as-synthesised NMC is 88 at% Ni, 5 at% Mn and 6 at% Co based on ICP-MS measurements, confirming that the composition is close to the targeted stoichiometry. An overview of the NMC and NMCA samples investigated by ICP-MS is given in Table S1, and all the tested samples have distributions close to their targeted values. The refined XRD pattern for NMC 750 °C is shown in Figure 1a, while an overview of all NMC, NMCA–Mn and NMCA–Co samples prepared at 750 °C, 800 °C and 850 °C is shown in Figure S1. The measurements indicate that phase pure layered α-$NaFeO_2$ type structures with R-3m space groups are achieved for all compositions and heat-treatment temperatures. The calculated levels of cation mixing from the Rietveld refinements are shown in Figure 1b and the c-lattice parameters are shown in Figure 1c. A complete overview of the calculated values from the Rietveld analysis is shown in Table S2. These results show the structural variations between the compositions and temperatures. All the samples prepared at 800 °C, and the NMC sample prepared at 750 °C, show low degrees of cation mixing at ~2 at %. NMCA–Co 750 °C shows the highest degree of cation mixing at ~5 at%, indicating a higher level of disorder in the structure. NMCA–Mn 750 °C and NMCA–Co 850 °C also show relatively high levels of anti-site disorder at ~3 at% compared to the 800 °C samples. The lattice parameter variations between the samples are low, with ~2 pm separating the largest and the smallest c-axis parameters. The lattice parameter variations can be due to a combination of factors, such as interior Li,[25–27] cation mixing[46] and ionic radii with respect to compositional differences.[53–55] From the Rietveld analysis, the c-axis lattice parameter is observed to increase with increasing heat-treatment temperature. The same trend can also be observed for the a-axis parameter in the 800–850 °C region. Following the observations of Li et al. for the $Li_{1+x}(Ni_yMn_{1-y})_{1-x}O_2$ system, the trend in lattice parameters may suggest some Li loss at higher temperatures.[56] The lattice parameters also differ between compositions, with the substitution of Co with Al having a notably greater effect than the substitution of Mn with Al. The relationship between unit cell axes lengths and transition metal substitution in doped NMC's is quite complex, with several factors possibly playing a role, including ionic size, charge compensation mechanisms, and bond dissociation energies.[57–59]

Figure 1d shows a magnified area 15° to 19° 2θ-region including the (101), (006) and (012) reflections of all three

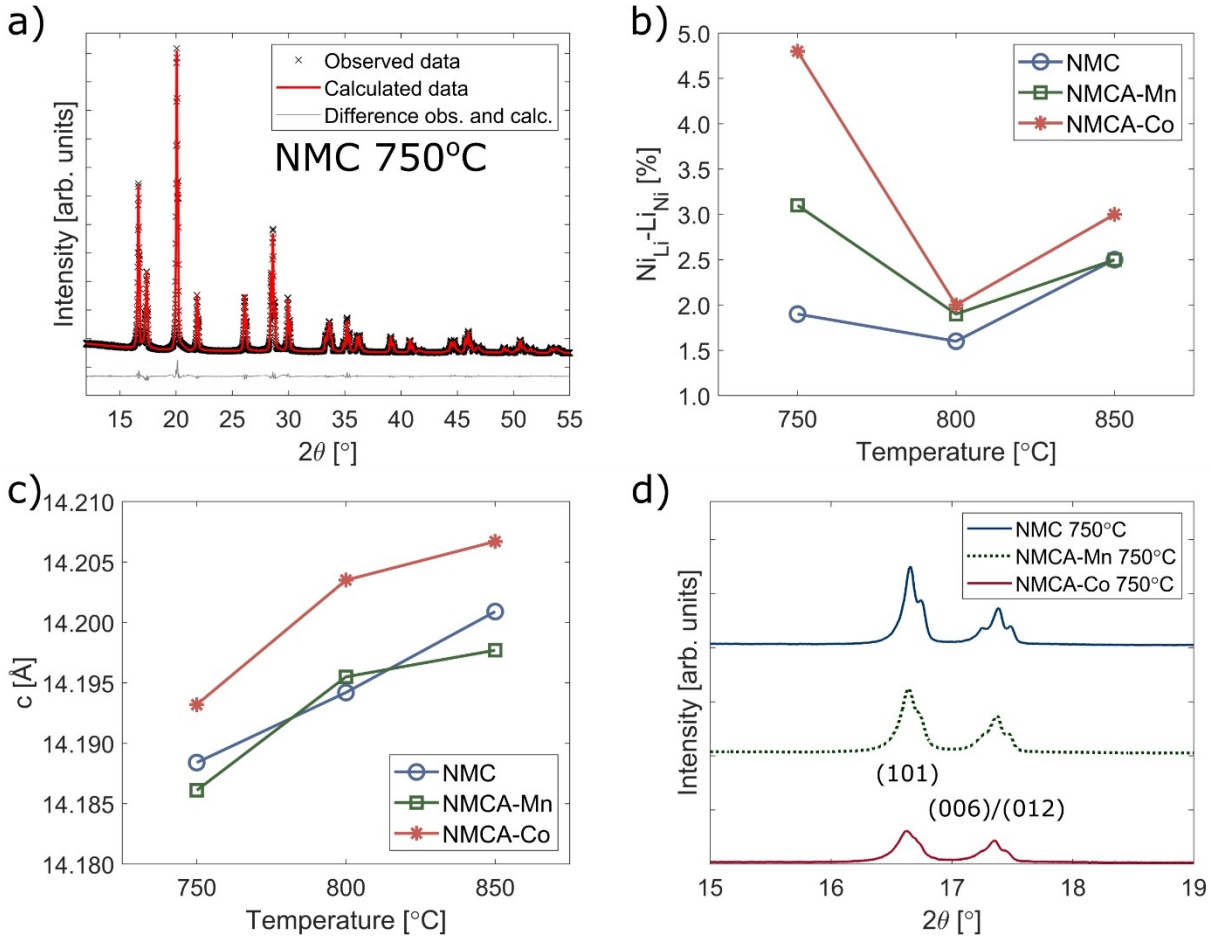

Figure 1. (a) Refined diffractogram of NMC 750 °C recorded with Mo-K_α radiation. (b) Calculated Li^+ and Ni^{2+} cation mixing amounts and (c) refined c-parameters. (d) Enlargement of (101), (006) and (012) reflections from the observed data sets of samples heat-treated at 750 °C.

compositions prepared at 750 °C. It can be seen that NMCA–Mn 750 °C and NMCA–Co 750 °C have broader reflections compared to NMC 750 °C as the (006)/(012) splittings and the $K\alpha_1$ and $K\alpha_2$ splittings are less visible. This broadening is an indication of either small or micro-strained crystallites in the NMCA–Mn 750 °C and NMCA–Co 750 °C samples. It was found that a model of microstrain-based peak broadening provided a substantially better fit than a crystallite size broading model (R_{wp} difference >1 for all samples). The calculated microstrain values for each refinement are shown in Table S2, and a clear correlation of microstrain with heat-treatment temperature is evident. Higher microstrain values are also calculated for the Al-doped samples (NMCA–Mn and NMCA–Co) prepared at 750 °C, which likely reflects poorer homogeneity due to slower cation diffusion kinetics. This also correlates with the calculated Li/Ni anti-site disorder, and the smaller grains and broader grain size distribution observed by SEM imaging (Figure 2). When increasing the heat-treatment temperature from 750 °C to 800 °C, the (006)/(012) splittings and the $K\alpha_1$ and $K\alpha_2$ splittings become more pronounced for NMCA (Figure S2), and similar levels of microstrain are calculated for all NMC and NMCA compositions.

The powder morphology was analysed by FESEM and the corresponding micrographs of the synthesised powders (Figure 2) show agglomerated primary particles with irregular shapes and increasing size with heat-treatment temperature for all three compositions. Although all samples have size distributions, typical primary particle sizes for NMC are 700 nm, 900 nm and 1.3 μm for 750 °C, 800 °C and 850 °C, respectively. NMCA–Mn and NMCA–Co have typical primary particle sizes of 200 nm, 800 nm and 1.5 μm for 750 °C, 800 °C and 850 °C, respectively.

NMCA–Mn and NMCA–Co prepared at 750 °C have large fractions of 200 nm-sized primary particles (Figure 2d,g and Figure S3), and the primary particles have sharp edges and corners. However, significant crystal growth can be seen when increasing the heat-treatment temperature, as seen in the NMCA–Mn and NMCA–Co 800 °C samples (Figure 2e,h). The large fraction of small primary particles for both NMCA samples prepared at 750 °C, as seen by the FESEM images, in addition to the higher degree of disorder in the structure, as indicated by the XRD results, suggest that the structures and morphologies have not properly equilibrated. Differing oxalate solubilities will inherently result in inhomogeneity at the precipitation and evaporation stages before the high temperature heat-treatment. The addition of Al^{3+}, with a small ionic radius ($r(Al^{3+}) = 53.5$ pm[15]) and a corresponding high charge density, seems to

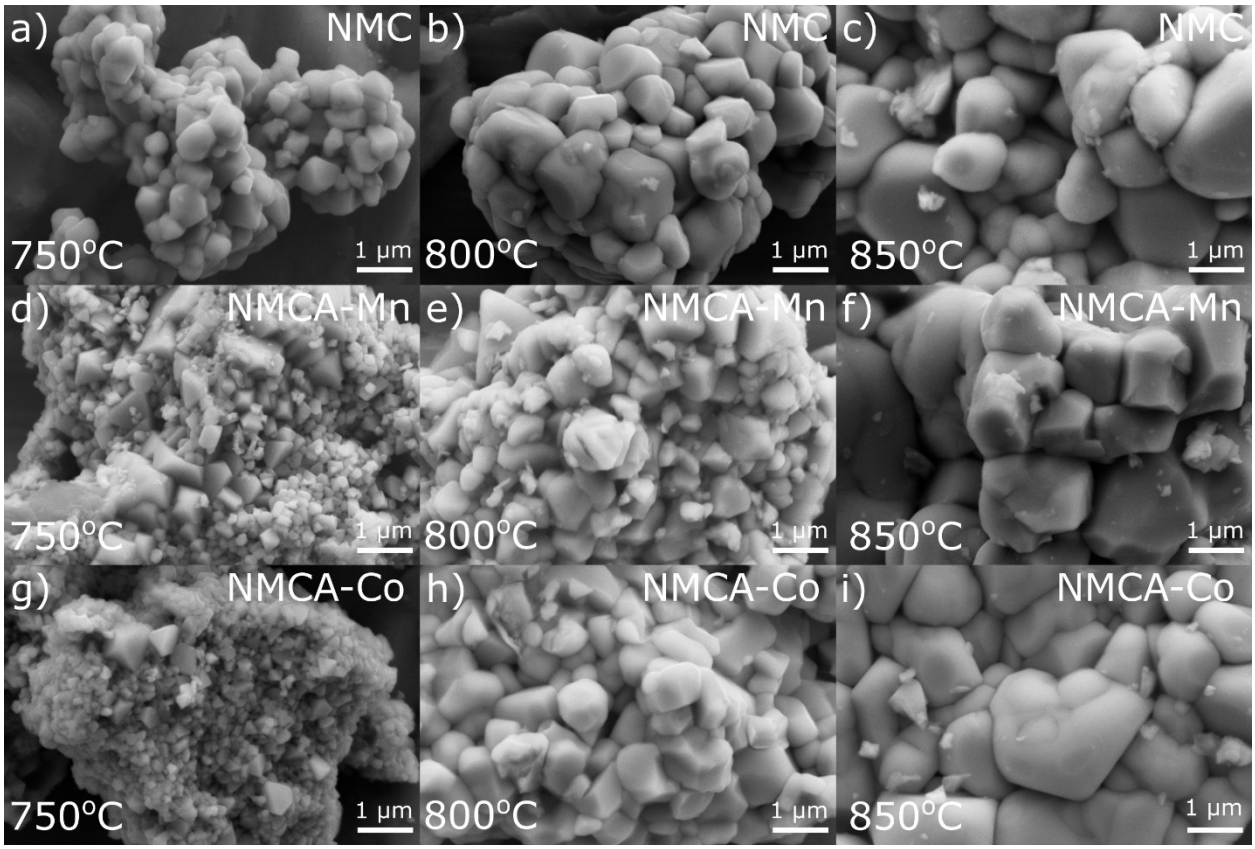

Figure 2. FESEM micrographs of (a-c) NMC, (d-f) NMCA–Mn and (g-i) NMCA–Co samples prepared at (a, d, g) 750 °C, (b, e, h) 800 °C and (c, f, i) 850 °C.

slow down the solid-state diffusion. It is likely that for the Al-containing compositions there is then some compositional inhomogeneity within the samples prepared at 750 °C, and possibly there is a compositional difference between the smaller and the larger primary particles as well. Raising the heat-treatment temperature from 750 °C to 800 °C clearly overcomes this mobility limitation, with larger primary particles and more ordered crystal structure, as observed by FESEM and XRD.

It is evident that from the FESEM images in Figure 2 that the primary particles are assembled into compact secondary particles. An overview FESEM image of NMCA–Co 800 °C (Figure S4) shows a large size distribution of secondary particles, and even some single crystals are observed (Figure S4b). A complete overview of low magnification FESEM images is shown in Figure S5, showing secondary particles. The size distribution may be a result of the synthesis route, but can also be due to deagglomeration of large secondary particles at poorly sintered connecting points as a consequence of mechanical stress, e.g. during sonication as part of the FESEM sample preparation. Neither the size nor the shape of these secondary particles of the powders could be accurately determined, as they may be affected by the FESEM sample preparation route. Further processing, such as the slurry mixing during the coating process, may also affect the secondary particle sizes in the final electrodes.

The first cycle capacities and coulombic efficiencies (CE) of half-cells cycled at 0.1 C and 3.0-4.3 V are given in Table S3. NMC 750 °C, NMCA–Mn 800 °C and NMCA–Co 800 °C have the highest discharge capacities of each composition at 185 mAh/g, 184 mAh/g and 179 mAh/g, respectively. All three materials have a similar first cycle inefficiency of 18%, which is believed to be caused by sluggish diffusion towards the end of the discharge process, as seen in other studies.[60–62] The second cycle potential profiles for NMC, NMCA–Mn and NMCA–Co prepared at 750 °C, 800 °C and 850 °C against Li-metal anodes are shown in Figure 3a–c. NMC 750 °C shows slightly higher discharge capacities compared to the Al-doped samples in the first and second cycles at 0.1 C. All the samples, except NMCA–Co 750 °C, show the characteristic potential plateaus of Ni-rich layered oxides due to the H1-M transition at ~3.7 V, the M–H2 transition at ~4.0 V, and the H2-H3 transition at ~4.2 V. These plateaus are highlighted in the derived incremental capacity plots (Figure S6). This is consistent with earlier work.[3,13,25,63] NMCA–Mn and NMCA–Co 750 °C show the lowest capacities and CE of their compositions. The potential profile of NMCA–Co 750 °C is smoother and without the characteristic plateaus of a Ni-rich layered oxide. In contrast, NMCA–Mn 750 °C shows the characteristic plateaus featured in Ni-rich layered oxides. The smoothening might be due to the higher degree of anti-site disorder of NMCA–Co 750 °C in comparison to NMCA–Mn 750 °C. The low capacities of both NMCA samples prepared at 750 °C are attributed the poor structures, with a high degree of cation mixing, and the fine-grained morphologies.

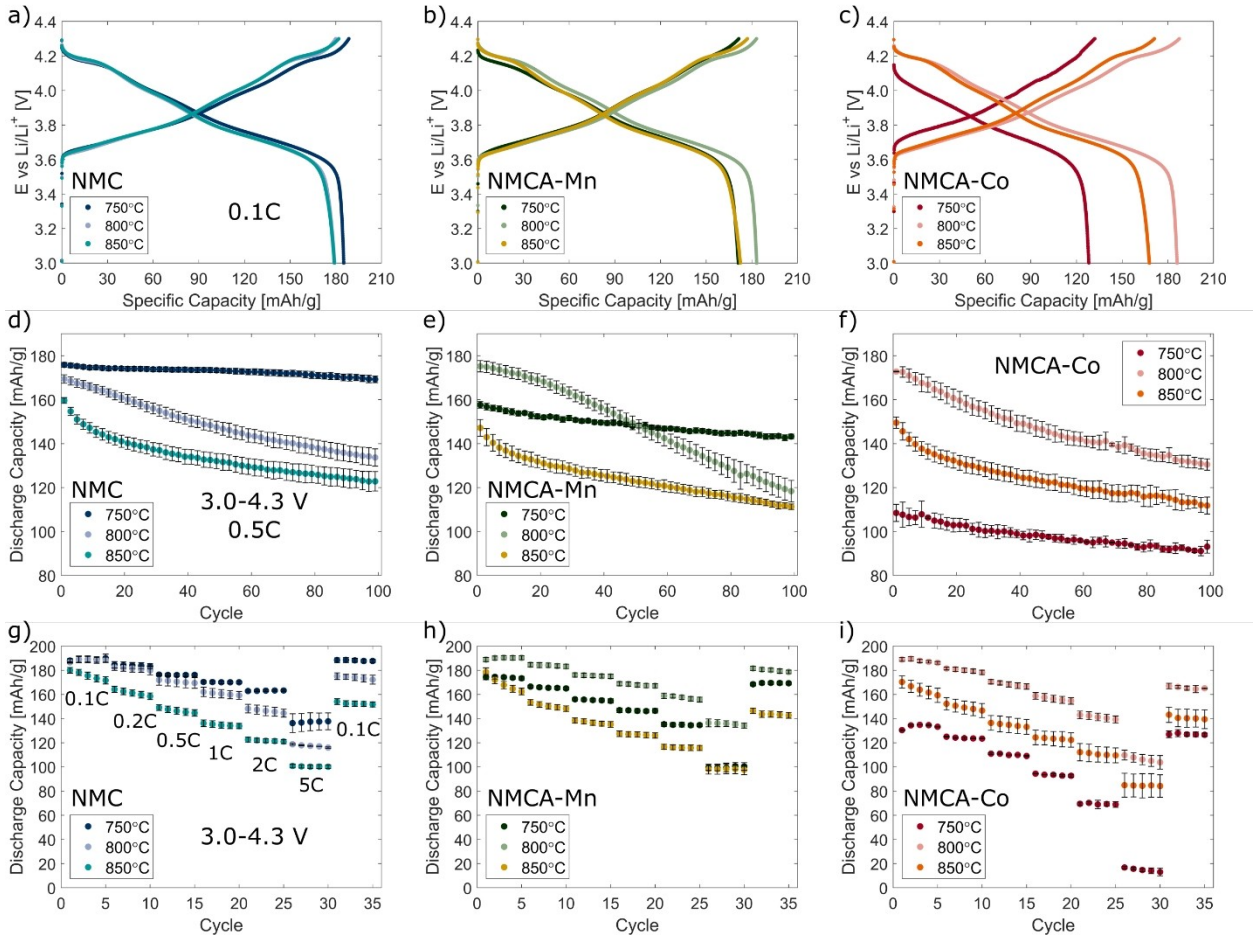

Figure 3. Electrochemical characterisation of (a, d, g) NMC, (b, e, h) NMCA–Mn and (c, f, i) NMCA–Co prepared at 750 °C, 800 °C and 850 °C in half-cell setup. (a–c) Second cycle potential profiles at 0.1 C, (d–f) 100-cycle test at 0.5 C, and (g-i) rate test with discharge rates from 0.1 C to 5 C. The cells were cycled between 3.0-4.3 V at 20 °C. The error bars indicate cell deviations. Each second cycle is plotted in the 100-cycle test.

Figure 3d–f and Table S4 show the performance over 100 cycles in half-cell setup at 0.5 C and 20 °C. NMC 750 °C, NMCA–Mn 800 °C and NMCA–Co 800 °C show the highest initial discharge capacities of their compositions at 176 mAh/g, 175 mAh/g and 173 mAh/g, respectively. These three materials show almost similar initial discharge capacities, but the cycling stabilities differ. NMC 750 °C shows a good capacity retention of 96% after 100 cycles. NMCA–Mn and NMCA–Co materials prepared at 800 °C fade considerably faster and respectively retain 67% and 75% of their initial capacity after 100 cycles. A similar fade was observed for the NMC sample prepared at 800 °C, which retained 79% of its initial capacity, and all samples heat-treated at 850 °C show reduced capacities when cycled at 0.5 C. This effect might be attributed to longer diffusion lengths in the large grains, and the possibility of limited Li-deficiency cannot be excluded. This highlights the importance of the heat-treatment conditions for Ni-rich layered oxides. Figure 3g–i shows the rate performance of NMC, NMCA–Mn, NMCA–Co prepared at 750 °C, 800 °C and 850 °C. NMC 750 °C and NMCA–Mn 800 °C show approximately similar rate performance, respectively retaining 73% and 71% of their capacity at 5 C as compared to at 0.1 C. NMC 750 °C also retains 99.5% of its initial capacity when returning to 0.1 C again after 30 cycles. NMCA–Co 800 °C shows an inferior rate performance as compared to NMC 750 °C and NMCA–Mn 800 °C. The lower rate performance of this sample might be attributed to the lower Co-content, as one third of the Co has been substituted with Al in the NMCA–Co samples, and this element is often associated with rate properties.[34,55]

Although NMC 750 °C shows good cycling stability, the achieved discharge capacity of 185 mAh/g at 20 °C and 0.1 C (18 mA/g), in a voltage window of 3.0-4.3 V, is low compared to earlier reported results. Initial capacities above 200 mAh/g at 19–25 °C have been reported for Ni-rich layered oxides with 85–90 at% Ni-content.[3,6,43,64,65] Higher capacities have also been reported with lower Ni-contents as well, such as above 190 mAh/g at 80 at% Ni.[3,37,66–69] It is known that Ni-rich layered oxides have poor storage characteristics, and are prone to reacting with H_2O and CO_2,[3,24,30,31] when exposed to air. In the work presented in Part A, the slurry preparation, tape casting, electrode cutting, and weighing was done outside a glovebox in air atmosphere. To assess the impact of this additional electrodes were processed with reduced air-exposure, with cutting and weighing was performed inside an Ar-filled glove-

box. Figure S7 shows how the potential profile of NMC 750 °C changes when the air exposure time is shortened. A capacity increase is clearly observed, and the average discharge capacity over the three formation cycles at 0.1 C increases from 186 mAh/g to 192 mAh/g. The improvement is attributed to reduced formation of Li impurity compounds on the particle surface. Table S5 shows selected reported discharge capacities and test parameters for Ni-rich layered oxides with 80–90 at% Ni, which are compared to those achieved this work.

In conclusion, NMC heat-treated at 750 °C showed the best overall electrochemical properties, with the highest discharge capacity, good rate capability, and the best capacity retention. The heat-treatment temperature of 750 °C was shown to be a key factor for stable cycling. Higher temperature heat-treatments were found to have a detrimental effect on electrochemical performance. Although NMCA–Mn and NMCA–Co 800 °C show similar degrees of Li/Ni anti-site disorder and similar initial electrochemical performance as NMC 750 °C, Al-doping did not improve electrochemical performance when implemented in this synthesis route and the NMCA 800 °C samples showed similar capacity fading to the undoped NMC parent composition prepared at 800 °C. This is in contrast to other studies where Al-doping has contributed to an improved cycling stability,[36–38] even when synthesised at temperatures down to at 730 °C.

Part B: The effect of excess Li precursor

The effect of excess Li precursor added in the synthesis on the physical and electrochemical properties of $LiNi_{0.88}Mn_{0.06}Co_{0.06}O_2$ (NMC) prepared at 750 °C was investigated. The contact time to ambient atmosphere of these materials was shortened to only the slurry mixing and coating process. It can be noted that NMC 750 °C and NMC 7.5 at% are similar in terms of composition, heat-treatment temperature and amount of Li precursor, but NMC 7.5 at% has been exposed to ambient atmosphere for a shorter time.

The physicochemical characterisation of the samples is shown in Figure S8. The refined XRD patterns of NMC prepared with 4 at%, 7.5 at% and 15 at% Li demonstrate α-$NaFeO_2$ structures with R-3m space group characteristic of layered oxide structures. All materials are phase pure, and no crystalline secondary phases containing Li (Li_2O, LiOH, Li_2CO_3) are observed, even when prepared with a 15 at% excess of Li precursor. However, excess Li that has not entered the structure nor evaporated may still exist on the particle surface as amorphous Li compounds. Rietveld refinements (Table S2) indicate low degrees of cation mixing between 2.1 % and 2.6 %. The lattice parameters show small variations, and the difference between the largest and the smallest c lattice parameters is ~1 pm. The lattice parameters decrease with increasing excess Li, which is consistent with Li et al..[56] FESEM micrographs show similar morphologies for all three samples, with the primary particles resembling those observed for the NMC 750 °C with primary particles between 400 nm and 700 nm. The transition metal distributions based on ICP-MS (Table S1) are close to the targeted stoichiometry, confirming the composition.

Figure 4a shows the second cycle potential profiles for NMC prepared with 4 at%, 7.5 at% and 15 at% excess Li cycled in half-cells at 0.1 C and 20 °C. The sample with 4 at% excess Li shows the highest capacity of 197±3 mAh/g, while the 15 at% Li excess sample shows the lowest capacity of 187±2 mAh/g. All three variations demonstrate the Ni-rich layered oxide characteristic potential plateaus. The discharge capacities at different C-rates in half-cells are shown in Figure 4b. It can be seen that the 4 at% excess sample has the highest discharge capacity up to 1 C, while the 7.5 at% excess sample has the highest discharge capacity above 1 C. All three variations retain 99 % of their initial discharge capacity when returning to a lower current again after 30 cycles of rate testing. Although the variations show very similar performance, the 15 at% excess Li sample shows slightly lower discharge capacities at all the current rates.

Cathode limited NMC||LTO cells were cycled 415 times to evaluate long-term cycling performance (Figure 4c) of NMC prepared with 4 at%, 7.5 at% and 15 at% excess Li at a controlled cycling temperature of 20 °C. LTO was used as anode instead of Li-metal to avoid cell degradation arising from the parasitic reactions between the electrolyte and Li-metal.[70] The three initial cycles at 0.1 C have average discharge capacities of 201 mAh/g, 195 mAh/g and 190 mAh/g for NMC 4 at%, 7.5 at% and 15 at%, respectively. After 104 cycles the respective NMC samples retain 98 %, 97 % and 94 % of their initial capacities. After 413 cycles the capacity retentions are reduced to 81 %, 83 % and 69 %, respectively. The higher capacities as compared to the NMC||Li cells can be explained by a small voltage window shift due to anodic overpotentials at the LTO anodes, shifting the anode potential slightly above 1.5 V vs Li/Li^+. The initial cycles at 0.5 C have discharge capacities 190 mAh/g, 187 mAh/g and 182 mAh/g for NMC 4 at%, 7.5 at% and 15 at%, respectively. After 412 cycles the respective NMC samples retain 74 %, 75 % and 57 % of their initial capacities. NMC 4 at% and 7.5 at% perform similarly in terms of both capacity and capacity retention, but NMC 4 at% has the higher capacities throughout the test. NMC 15 at% shows consistently the lowest capacity and fades considerably faster. High CEs of ~99.9 % are seen for all three samples throughout the test.

The development of the potential profiles (Figure 5 and Figure S9) shows the changing polarisation of the NMC||LTO cells upon cycling. Higher polarisation is seen in the 15 at% sample in comparison to the 4 at% sample. The polarisation is also more pronounced at 0.5 C than 0.1 C due to the kinetic contribution, as seen in Figure S9. In the 15 at% sample, the H2-H3 phase transition usually seen as a voltage plateau at ~2.7 V (~4.2 V vs Li/Li^+) cannot be seen after 300 cycles at 0.1 C and after 200 cycles at 0.5 C. This is attributed the fact that the NMC||LTO cells polarise and reach the upper cut-off voltage before enough Li has been extracted from the NMC cathodes for the phase transition to occur. NMC 4 at% and NMC 15 at% are the best and worst performing samples, respectively, based on discharge capacity, polarisation and cycling stability. These

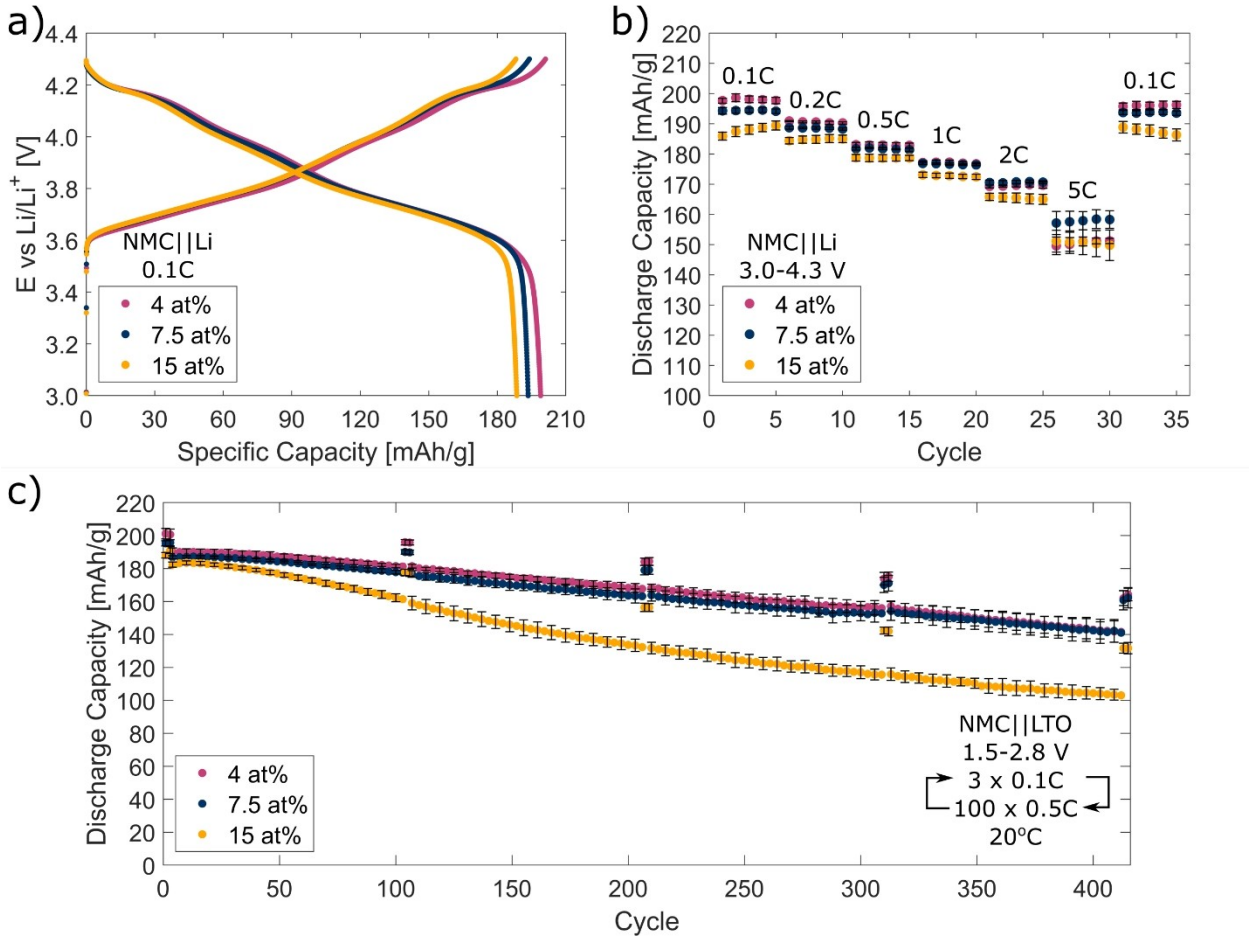

Figure 4. Electrochemical characterisation of NMC prepared with 4 at%, 7.5 at% and 15 at% excess Li precursor at 750 °C. (a) Second cycle potential profiles at 0.1 C and (b) rate test with discharge rates from 0.1 C to 5 C were cycled against a Li-metal anode between 3.0–4.3 V. (c) Long-term cycling test at 0.1 C and 0.5 C against a LTO anode between 1.5–2.8 V. The error bars indicate cell deviations. In the long-term cycling test, each third cycle is plotted in the 0.5 C region, and each second of these cycles have error bars. The first and third cycles in the 0.1 C region are plotted. All tests were done at 20 °C.

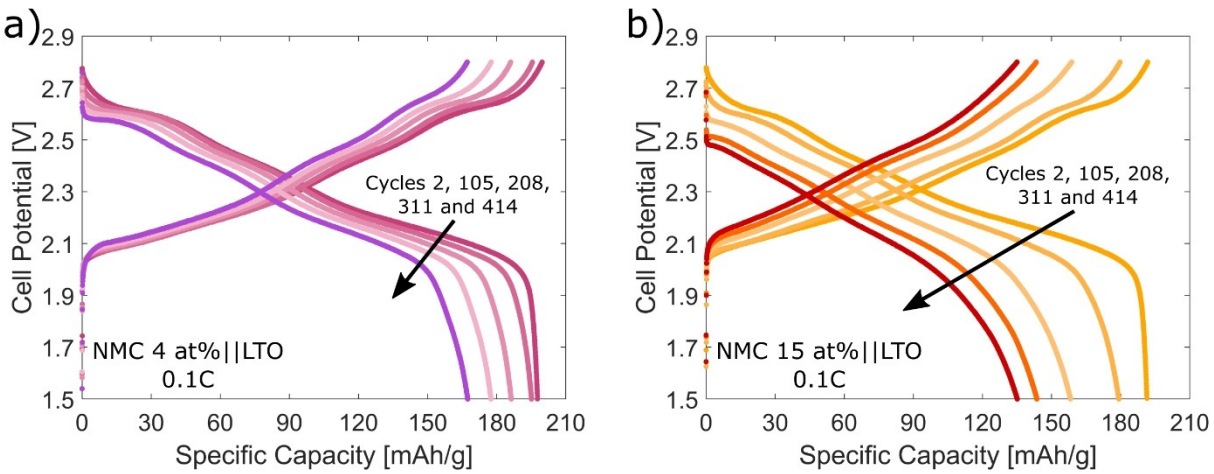

Figure 5. Potential profiles of selected 0.1 C cycles from the long-term cycling test seen in Figure 4c for (a) NMC 4 at% and (b) NMC 15 at%. NMC was cycled against a LTO anode at 20 °C.

two samples were investigated further to probe the failure mechanisms.

A cycled NMC 15 at% cathode, the poorest performing sample, was removed and examined by XRD to study the state of the crystal structure after 415 cycles, and if there are clear

signs of structural deterioration. The XRD diffractograms (Figure S10) show no unexpected additional peaks for the cycled cathode as compared to the pristine cathode. The diffraction pattern indicates that the layered oxide structure is still present after 415 cycles in the bulk material. Additional peaks can be traced back to either the Al-foil current collector or the XRD sample holder.

NMC cathodes from cycled NMC||LTO cells were reassembled into half-cell configuration with fresh Li-metal anodes and refilled with electrolyte to investigate if Li loss, anode degradation or electrolyte consumption contributes to the NMC||LTO cell degradation. The cycled NMC cathodes were removed after being discharged to 1.5 V versus LTO (~3.0 V versus Li/Li^+), but the open circuit voltages of the reassembled NMC||Li cells were measured to 3.6 V for both NMC 4 at% and 15 at%. These open circuit voltages are higher as compared NMC||Li cells with pristine NMC cathodes. Further discharge of the reassembled cells achieved only 3.4 mAh/g and 5.6 mAh/g for NMC 4 at% and 15 at%, respectively. This accounts for 1.7% and 3.0% of their initial discharge capacities, respectively. In total, NMC 4 at% and 15 at% respectively lost 38 mAh/g and 59 mAh/g of their capacities over 415 cycles based on the 0.1 C capacities, and then only regain ~10% of the lost capacity from this discharge with refilled electrolyte and a fresh Li-metal anode. A full charge-discharge cycle in the reassembled half-cells at 0.1 C led to similar capacities as their last full-cell cycle (Figure S11). Hence, Li inventory loss cannot explain the loss in reversible capacity. It is also unlikely that the degradation of the NMC||LTO cells is caused by the LTO anodes or electrolyte, but rather by degradation of the active NMC cathode materials.

Cross-sectional imaging was used to inspect cycled NMC cathodes for microcracking and morphology changes. Figure 6 displays cross-sections of pristine and cycled NMC 4 at% and NMC 15% cathodes. The secondary particles of both NMC 4 at% and NMC 15 at% have irregular shapes after the cathode laminate fabrication. The cross-section image of cycled NMC 15 at% shows the only observed crack in the samples, but the cross-section appears intact to a large degree. However, these

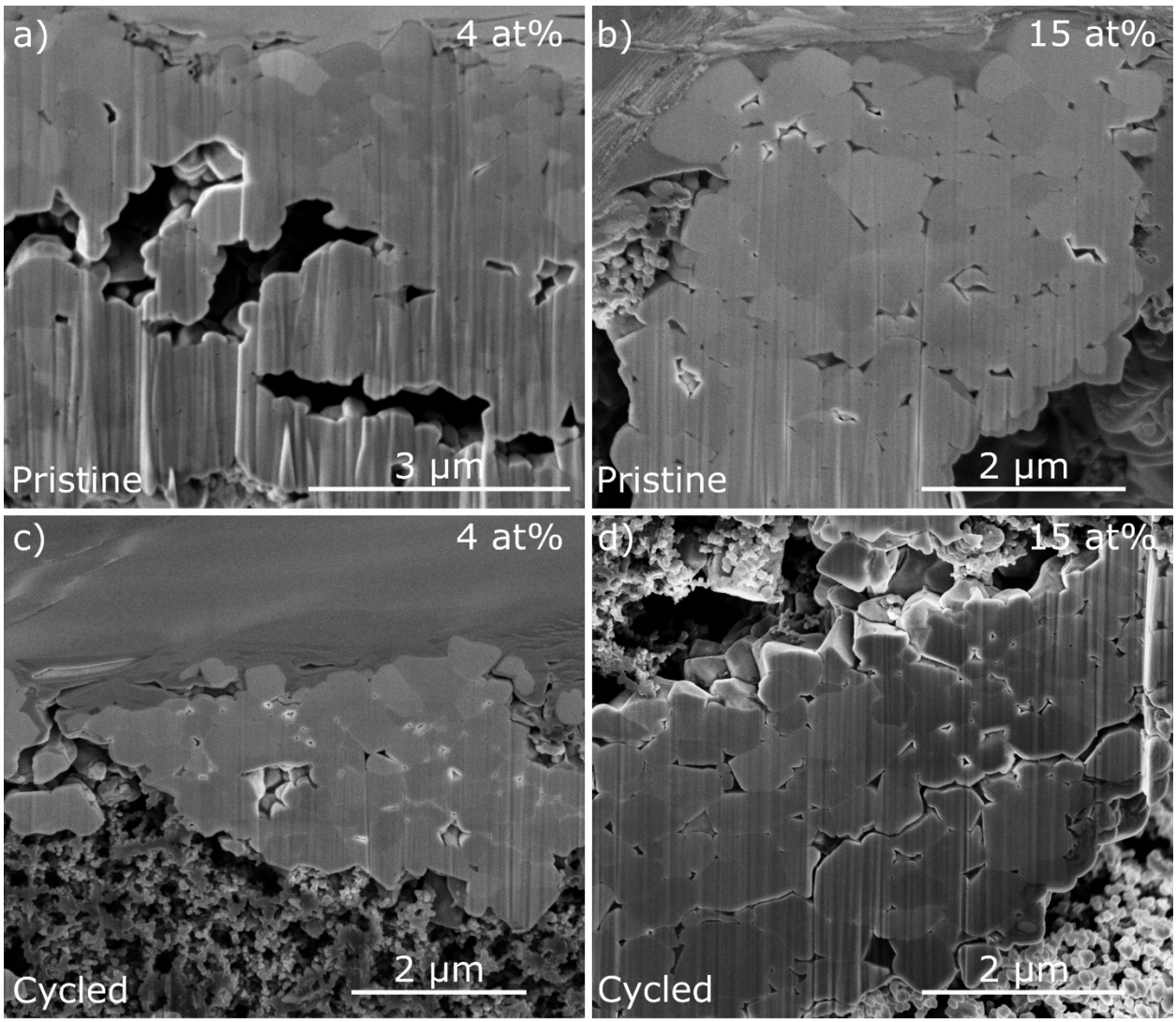

Figure 6. Cross-section FIB-SEM images of (a, c) NMC 4 at% and (b, d) NMC 15 at% cathodes (a, b) before and (c, d) after 415 cycles in NMC||LTO cells, as reported in Figure 4c.

images are based on 20 µm cross-sections and more cracks are expected across the entire cathode. Such cracking is attributed the repeated anisotropic volume changes happening during (de)lithitation.[28,71,72] NMC 15 at% (Figure 6b,d) shows a higher intergranular porosity in the agglomerated secondary particles than NMC 4 at% (Figure 6a,c) when comparing both the pristine and cycled cross-sections images. This might be directly correlated with excess Li species added during synthesis accumulating at the surface of the crystallites before evaporating at high temperature. Such porosity is expected to make the material more prone to cracking. It is also plausible that these pores expand in a highly charged and delithiated state.[73] In addition, if these pores can form interconnected channels, they can allow for electrolyte penetration into the interior of the secondary particles, exposing more surface area to electrolyte. Fresh surface exposed to electrolyte can proceed to surface reconstruction reactions[6,12,27] and parasitic reactions forming CEI.[6]

The evolution of impedance for the NMC 4 at% and NMC 15 at% upon cycling was studied in order to identify factors contributing to material degradation and capacity fade. Cells were cycled at 1 C and PEIS measurements were taken in a semi-charged state at 4.1 V versus Li/Li$^+$ after 2, 40 and 80 cycles in a three-electrode test cell in order to avoid increased impedance contributions from the Li-metal counter electrode. Figure S12 shows the discharge capacities upon cycling and Figure 7 shows the PEIS spectra in Nyquist representation. In these plots, the zero intercept with the horizontal axis at high frequencies is attributed the ohmic resistance (R_e), the semi-circle at high frequencies is attributed to surface film resistance (R_{sf}), the semi-circle at medium frequencies is attributed to charge transfer resistance (R_{ct}) between the electrolyte and electrode, and the tail at low frequencies is attributed the Warburg diffusion element (Z_w).[28,74–78] The calculated values from the data fitting are shown Table S6. It is noted that lowest frequencies have not been included in the data fitting in this work, and accordingly the Warburg element has been excluded. This might have a minor effect on the reported values, but not on the observed trend with increasing resistance over the cycles. Several factors can contribute to the charge transfer resistance, and it is often associated with surface structure degradation and the growth of the surface reconstruction layer.[6,21,28,79] Both samples show impedance growth, but of different character. The impedance growth in NMC 4 at% is mainly due to the surface film, while the charge transfer resistance is very low throughout the cycling program. This may suggest a growing CEI layer, while the surface structure stays to a high degree intact. The impedance growth in NMC 15 at% has contributions from both increased surface film and charge transfer resistances. It is interesting that NMC 4 at% shows a larger surface film resistance as it is expected that there are more Li compounds present on the NMC 15 at% surface. However, this might be explained by Li_2CO_3 decomposition during cycling. Jung et al. observed CO_2 gas evolution from NMC 811 between 4.0-4.2 V versus Li/Li$^+$ believed to be decomposition of residual carbonates from the synthesis,[23] which is within the voltage cut-off limits used in this study. The evolution of the charge transfer resistance in NMC 15 at% may suggest surface degradation impeding Li$^+$ transfer between the electrode and electrolyte. A general trend for both samples is a decreasing capacitance (C_{sf} and C_{ct}) upon cycling, which is evidence of a decrease in active surface area of the electrode. This might suggest a loss of active material instead of an increase in surface area caused by cracking or increased porosity. The total resistances of both samples are close in magnitude although NMC 4 at% outperforms NMC 15 at% in terms of capacity and stability. The origin of the inductive loop observed between the two semi-circles in NMC 15 at% cycle 80 is not known, but inductive loops in half-cells have previously been shown to originate from experimental artefacts.[80] Alternatively, adsorption reactions in general have been shown to result in inductive loops.[81]

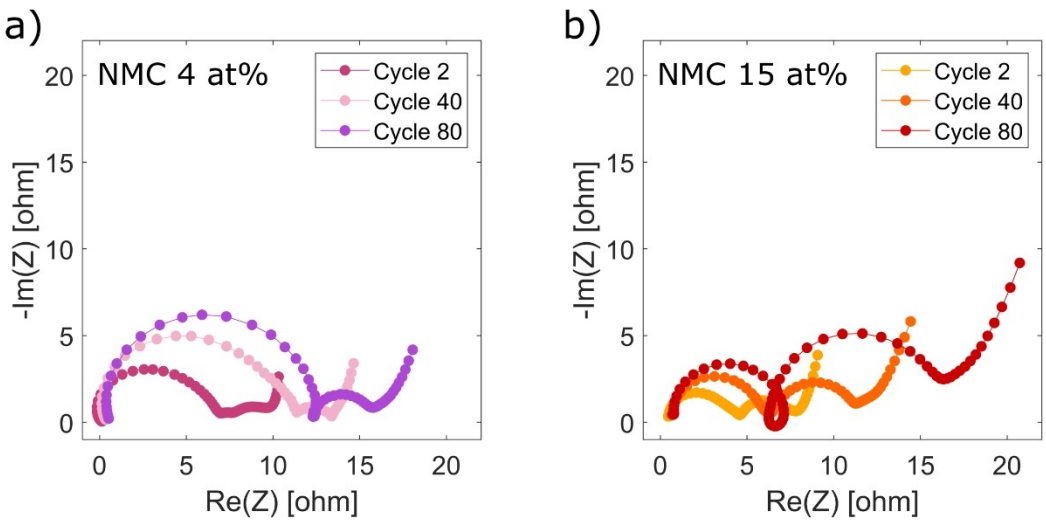

Figure 7. Nyquist plots of (a) NMC 4 at% and (b) NMC 15 at%. The cells were cycled with a Li-metal anode at 1 C and 20 °C. The cells were charged at 0.05 C to 4.1 V before the EIS measurements.

Conclusion

Ni-rich NMC and NMCA materials with 88 at% Ni were synthesised through a single-pot oxalic acid co-precipitation. An acidic environment allowed for all cation elements, including Li and Al, to be added in the co-precipitation step. NMCA variations were investigated with 2 at% Al-doping substituting either Mn or Co. Both NMC and NMCA materials were tested with a broad span of heat-treatment temperatures, and the importance of both the degree of Li-excess in the precursors and the heat-treatment regime is highlighted in the structural and electrochemical evaluations. All synthesised materials were phase pure and polycrystalline. A low degree of Ni^{2+} in the Li-layer in NMC was achieved already at 750 °C, while NMCA needed a higher temperature of 800 °C to achieve a similar well-ordered structure and crystal growth. Although the NMC and NMCA materials showed similar initial electrochemical performance, the addition of Al^{3+} did not improve the electrochemical cycle life when implemented through the synthesis route and parameters used in this work. The effect of excess Li precursor amounts was further evaluated using the undoped NMC heat-treated at 750 °C. At 4 at% excess Li precursor, the lowest amount tested in this study, NMC had a good capacity and cycle life. Long-term cycling of this material in NMC||LTO cells showed an initial capacity of 201 mAh/g at 0.1 C in a window of 1.5-2.8 V at 20 °C, with 81 % capacity retention after 415 cycles. Post-mortem investigations indicate that capacity fade is connected to the changes in the NMC cathode, and that Li inventory loss is not the main cause of fading. Cross-sectional imaging of this material does not show significant micro-cracking. The material showed a low charge transfer resistance growth, possibly due to a low degree of surface structural damage. Using a high amount of 15 at% excess Li precursor proved detrimental to the electrochemical performance. The work shows that Ni-rich layered oxide polycrystalline materials can be stabilised by optimising composition and synthesis parameters without an additional surface modification.

Experimental Section

Synthesis of Ni-rich layered oxides

Ni-rich layered oxides $LiNi_{0.88}Mn_{0.06}Co_{0.06}O_2$ (NMC), $LiNi_{0.88}Mn_{0.04}Co_{0.06}Al_{0.02}O_2$ (NMCA–Mn) and $LiNi_{0.88}Mn_{0.06}Co_{0.04}Al_{0.02}O_2$ (NMCA–Co) were synthesised through a single-pot oxalic acid co-precipitation route. As precursors $LiNO_3$ (99 %, Alfa Aesar), $Ni(CH_3COO)_2{*}4H_2O$ (≥98 %, Alfa Aesar), $Mn(CH_3COO)_2{*}4H_2O$ (≥99 %, Merck), $Co(CH_3COO)_2{*}4H_2O$ (≥98 %, Sigma-Aldrich), and $Al(NO_3)_3{*}9H_2O$ (≥98 %, Sigma-Aldrich) were used. As precipitation medium oxalic acid ($C_2H_2O_4$, 98 %, Aldrich and Alfa Aesar) was used, as well as HNO_3 (Sigma-Aldrich) and NH_3 (VWR) for pH adjustment. 50 mmol of Ni-rich layered oxide materials were synthesised per batch. First, the metal ion solution was prepared by dissolving the corresponding precursors in 500 mL ethanol/deionised water 1 : 1 by volume at pH 3 and temperature of 60 °C. Ni, Mn, Co and Al precursors were added in stoichiometric amounts, while Li precursor was added at a 4 at%, 7.5 at% and 15 at% excess. The precipitation solution was prepared by dissolving 208 mmol oxalic acid under the same conditions and same amount of solvent as described above. The amount of oxalic acid corresponds to approximately 2.7 times the oxalate needed to precipitate all the metal ions as simple oxalates. The oxalic acid solution was stirred at 300 rpm and 60 °C while the metal ion solution was added at a dripping rate of approximately 0.1 mL per second using a dropping funnel. The pH was readjusted to pH 3 at intervals of 30 minutes during precipitation. The precipitate was aged for 19 hours under constant stirring before the solvent was evaporated on a heating plate at 150 °C. The dry precipitate was ground and calcined in air at 450 °C for 5 hours to burn off organic residues. Afterwards, the calcined powder was reground and heat-treated in flowing O_2 atmosphere at 750 °C, 800 °C and 850 °C with a dwell time of 15 hours. A heating rate of 200 °C per hour and a cooling rate of 300 °C per hour were used. The final powder material was reground and sieved to 50 μm.

Physicochemical characterisation

The crystal structures and phase purities were investigated by powder x-ray diffraction (XRD) on a Bruker D8 A25 DaVinci X-ray Diffractometer operating with a Mo-K_α radiation ($\lambda = 0.71$ Å) source, focussing Göbel mirror, and equipped with a LynxEye™ XE 1D Detector. Samples were loaded into 0.3 mm diameter quartz capillaries and data collected in transmission mode. Post-mortem XRD investigations of cycled cathodes were measured in Bragg-Brentano geometry with Cu-K_α radiation ($\lambda = 1.54$ Å), using a Bruker D8 A25 DaVinci X-ray Diffractometer with LynxEye™ XE 1D Detector.

Structural analysis was performed via Rietveld refinement using TOPAS (version 5, Bruker AXS). A fundamental parameters model of peak shape broadening was derived using a reference diffraction pattern collected for NIST SRM 640d. The refinements were based on a rhombohedral α-$NaFeO_2$ structural model, with R-3m space group and Li placed in the 3a position, Ni, Mn, Co and Al in the 3b position and O in the 6c position. The refinements assumed fully stoichiometric samples and a model in which Li and Ni were free to switch positions (cation mixing) while Mn, Co and Al were confined to the TM-layer. The a and c lattice parameters were treated as variables, as was O z coordinate, and linewidths were modelled within the fundamental parameters approach assuming micro-strain-type broadening. It is noted that the use of short wavelength radiation causes a shift of the diffraction pattern to lower angles of 2θ compared to Cu-K_α radiation ($\lambda = 1.54$ Å), allowing the inclusion of a large number of reflexes in the refinement, but resulting in a high degree of asymmetry in the (003) diffraction reflex that was found difficult to accurately model in refinements. Accordingly, that reflex was excluded from the refinements.

The particle morphology was investigated by field emission scanning electron microscopy (FESEM) on a ZEISS SUPRA 55VP or a ZEISS ULTRA 55 operating in secondary electron mode. Elemental composition was analysed by inductively coupled plasma mass spectroscopy (ICP-MS). Powder samples were first dissolved in Aqua Regia (HNO_3 and HCl) or HNO_3 and HF at 240 °C in a Milestone UltraWAVE microwave oven, and then analysed in an Agilent 8800 Triplet Quadropole ICP-MS.

Cross-sectional imaging of pristine and cycled cathodes was performed by focused ion beam scanning electron microscope (FIB-SEM) on a FEI Helios NanoLab DualBeam FIB. Cross-sections were prepared by Ga-ion milling with a protective Pt-layer and were imaged in secondary electron mode. Cathodes from disassembled cells were rinsed with dimethyl carbonate (DMC, Sigma-Aldrich) before post-mortem measurements.

Electrochemical characterisation

A slurry consisting of 85 wt% Ni-rich layered oxide powder, 10 wt% carbon black (Imerys Super C65) and 5 wt% PVDF (Kynar) in N-methyl-2-pyrrolidone (NMP, Sigma-Aldrich) was homogenised in a mixer mill (Retsch M3) and tape casted onto Al-foil using a 150 μm fixed gap applicator. The as-formed cathode sheets were dried in a furnace at 80 °C for 30 minutes to remove the majority of NMP solvent before being vacuum dried at 120 °C for 12 hours. The dried laminates were then transferred to an Ar atmosphere glovebox (MBraun, <0.1 ppm H_2O and <0.1 ppm O_2). Circular disk cathodes were cut and assembled into 2016 coin cells with Li-metal or oversized $Li_4Ti_5O_{12}$ (LTO; 2 mAh/cm^2; CUSTOMCELLS®) anodes. Loadings were typically ~4 mg_{NMC}/cm^2. Polyolefin tri-layer Celgard 2325 separators soaked in 1 M $LiPF_6$ in ethylene carbonate and ethylene methylene carbonate (EC/EMC; 1:1 by volume; Sigma-Aldrich) acted as separator and electrolyte, respectively. The details regarding dimensions of the cathode and anode disks, in addition to the amount of electrolyte are specified in Table S7. The cells were rested for 24 hours between assembly and electrochemical testing. Electrochemical testing of coin cells was performed on BioLogic BCS-805 and Lanhe CT2001A systems with various battery testing programs. Cells with Li-metal anodes were cycled between 3.0-4.3 V, while cells utilising LTO anodes were cycled between 1.5–2.8 V (based on LTO having a nominal voltage of 1.5 V versus Li/Li^+). Cells were cycled at various currents based on 1 C being 180 mA/g. Cycling at discharging rates up to 0.5 C was combined with equal charging rates, while cycling at discharging rates above 0.5 C was combined with 0.5 C charging rates. All the charging processes included a constant voltage step at the upper cut-off potentials until the current had decayed to 0.1 C. Three formation cycles at 0.1 C were completed before the 100-cycle test program at 0.5 C. The figures and tables contain averaged values of 2–4 coin cells, specified in Table S7, and their standard deviations are indicated by error bars.

Selected cycled cells were disassembled and their cathodes and separators were reassembled to new coin cells. The separators were not removed in order to avoid damaging the cycled cathodes. The new cells had a fresh Li-metal anode, an additional separator and were refilled with 50 μL electrolyte.

PAT-cells (EL-CELL®) were assembled for potentiostatic electrochemical impedance spectroscopy (PEIS) measurements. These cells consisted of a Ni-rich layered oxide working electrode, Li-metal reference and counter electrodes, glass fibre separators (260 μm) and 100 μL of the same electrolyte as used for the coin cell measurements. The cells were cycled between 3.0–4.3 V versus Li/$Li^+_{reference}$ and with one formation cycle at 0.1 C. The cells were cycled at 1 C discharging- and charging rates, and with a constant voltage step at the upper cut-off potential until a current decay to 0.1 C. PEIS measurements were taken in a semi-charged state of 4.1 V in cycle 2, 40 and 80. During these three cycles the cells were charged to 4.1 V at 0.05 C and held at the upper cut-off potential for 10 hours to equilibrate the cells. The PEIS measurements were performed with 5 mV amplitude from 200 kHz to 10 mHz using a BioLogic VMP-300 potentiostat. The measured PEIS data from 200 kHz to 400 mHz was by fitted to an equivalent circuit shown in Figure S13 in BT-lab software (V1.65).

Acknowledgements

The Research Council of Norway is acknowledged for financial support of the HiCath project (grant number 280910) and for the support to the Norwegian Micro- and Nano-Fabrication Facility, NorFab (grant number 245963). Marianne Kjos is acknowledged for ICP-MS analyses. Per Erik Vullum is acknowledged for assistance with cross-section FIB-SEM imaging.

Conflict of Interest

The authors declare no conflict of interest.

Data Availability Statement

The data that support the findings of this study are available from the corresponding author upon reasonable request.

Keywords: Electrochemical characterisation · Li-ion batteries · Ni-rich layered oxides · Physicochemical characterisation · Synthesis

[1] N. Nitta, F. Wu, J. T. Lee, G. Yushin, *Mater. Today* **2015**, *18*, 252–264.
[2] J.-M. Tarascon, M. Armand, *Nature* **2001**, *414*, 359–367.
[3] H.-J. Noh, S. Youn, C. S. Yoon, Y. K. Sun, *J. Power Sources* **2013**, *233*, 121–130.
[4] S.-M. Bak, E. Hu, Y. Zhou, X. Yu, S. D. Senanayake, S. J. Cho, K.-B. Kim, K. Y. Chung, X.-Q. Yang, K.-W. Nam, *ACS Appl. Mater. Interfaces* **2014**, *6*, 22594–22601.
[5] K.-S. Lee, S.-T. Myung, K. Amine, H. Yashiro, Y.-K. Sun, *J. Electrochem. Soc.* **2007**, *154*, A971–A977.
[6] H.-H. Sun, A. Manthiram, *Chem. Mater.* **2017**, *29*, 8486–8493.
[7] W. Li, E. M. Erickson, A. Manthiram, *Nat. Energy.* **2020**, *5*, 26–34.
[8] R. Schmuch, R. Wagner, G. Hörpel, T. Placke, M. Winter, *Nat. Energy.* **2018**, *3*, 267–278.
[9] T. Daly, Y. Sun, "China's CATL starts mass production of high-nickel batteries: chairman" available at https://www.reuters.com/article/us-china-batteries-catl/chinas-catl-starts-mass-production-of-high-nickel-batteries-chairman-idUSKCN1S60YM, **2019**.
[10] K. Mizushima, P. C. Jones, P. J. Wiseman, J. B. Goodenough, *Mater. Res. Bull.* **1980**, *15*, 783–789.
[11] T. Ohzuku, A. Ueada, M. Nagayama, *J. Electrochem. Soc.* **2006**, *140*, 1862–1870.
[12] W. Liu, P. Oh, X. Liu, M.-J. Lee, W. Cho, S. Chae, Y. Kim, J. Cho, *Angew. Chem. Int. Ed.* **2015**, *54*, 4440–4457; *Angew. Chem.* **2015**, *127*, 4518–4536.
[13] W. Li, J. N. Reimers, J. R. Dahn, *Solid State Ionics* **1993**, *67*, 123–130.
[14] T. A. Hewston, B. L. Chamberland, *J. Phys. Chem. Solids* **1987**, *48*, 97–108.
[15] R. D. Shannon, *Acta Crystallogr.* **1976**, *32*, 751–767.
[16] Z.-Y. Li, H. Guo, X. Ma, K. Sun, D. Chen, L. He, S. Han, *J. Phys. Chem. C* **2019**, *123*, 19298–19306.
[17] A. Rougier, I. Saadoune, P. Gravereau, P. Willmann, C. Delmas, *Solid State Ionics* **1996**, *90*, 83–90.
[18] N. Y. Kim, T. Yim, J. H. Song, J.-S. Yu, Z. Lee, *J. Power Sources* **2016**, *307*, 641–648.
[19] N. Phattharasupakun, M. M. E. Cormier, E. Lyle, E. Zsoldos, A. Liu, C. Geng, Y. Liu, H. Li, M. Sawangphruk, J. R. Dahn, *J. Electrochem. Soc.* **2021**, *168*, 090535.
[20] K. Kang, G. Ceder, *Phys. Rev. B: Condens. Matter Mater. Phys.* **2006**, *74*, 094105.
[21] F. Lin, I. M. Markus, D. Nordlund, T.-C. Weng, M. D. Asta, H. L. Xin, M. M. Doeff, *Nat. Commun.* **2014**, *5*, 3529.
[22] S. Hwang, W. Chang, S. M. Kim, D. Su, D. H. Kim, J. Y. Lee, K. Y. Chung, E. A. Stach, *Chem. Mater.* **2014**, *26*, 1084–1092.
[23] R. Jung, M. Metzger, F. Maglia, C. Stinner, H. A. Gasteiger, *J. Phys. Chem. Lett.* **2017**, *8*, 4820–4825.
[24] T. Hatsukade, A. Schiele, P. Hartmann, T. Brezesinski, J. Janek, *ACS Appl. Mater. Interfaces* **2018**, *10*, 38892–38899.
[25] H. Li, N. Zhang, J. Li, J. R. Dahn, *J. Electrochem. Soc.* **2018**, *165*, A2985–A2993.

[26] W. Li, H. Y. Asl, Q. Xie, A. Manthiram, *J. Am. Chem. Soc.* **2019**, *141*, 5097–5101.
[27] H.-H. Ryu, K.-J. Park, C. S. Yoon, Y. K. Sun, *Chem. Mater.* **2018**, *30*, 1155–1163.
[28] C. S. Yoon, D.-W. Jun, S.-T. Myung, Y.-K. Sun, *ACS Energy Lett.* **2017**, *2*, 1150–1155.
[29] J. Li, J. Harlow, N. Stakheiko, N. Zhang, J. Paulsen, J. Dahn, *J. Electrochem. Soc.* **2018**, *165*, A2682–A2695.
[30] S. W. Doo, S. Lee, H. Kim, J. H. Choi, K. T. Lee, *ACS Appl. Energ. Mater.* **2019**, *2*, 6246–6253.
[31] R. Jung, R. Morasch, P. Karayaylali, K. Phillips, F. Maglia, C. Stinner, Y. Shao-Horn, H. A. Gasteiger, *J. Electrochem. Soc.* **2018**, *165*, A132–A141.
[32] H. S. Liu, Z. R. Zhang, Z. L. Gong, Y. Yang, *Electrochem. Solid-State Lett.* **2004**, *7*, A190.
[33] C. Busà, M. Belekoukia, M. J. Loveridge, *Electrochim. Acta* **2021**, *366*, 137358.
[34] H.-H. Sun, W. Choi, J. K. Lee, I.-H. Oh, H.-G. Jung, *J. Power Sources* **2015**, *275*, 877–883.
[35] J. Zheng, W. H. Kan, A. Manthiram, *ACS Appl. Mater. Interfaces* **2015**, *7*, 6926–6934.
[36] N.-Y. Park, H.-H. Ryu, G.-T. Park, T.-C. Noh, Y.-K. Sun, *Adv. Energy Mater.* **2021**, *11*, 2003767.
[37] N. P. Wagner, J. R. Tolchard, A. Tron, H. N. Pollen, H. Gaertner, P. E. Vullum, *MRS Adv.* **2020**, 1–8.
[38] U.-H. Kim, L.-Y. Kuo, P. Kaghazchi, C. S. Yoon, Y.-K. Sun, *ACS Energy Lett.* **2019**, *4*, 576–582.
[39] H. Li, M. Cormier, N. Zhang, J. Inglis, J. Li, J. R. Dahn, *J. Electrochem. Soc.* **2019**, *166*, A429–A439.
[40] M. M. E. Cormier, N. Zhang, A. Liu, H. Li, J. Inglis, J. R. Dahn, *J. Electrochem. Soc.* **2019**, *166*, A2826–A2833.
[41] F. Xin, H. Zhou, Y. Zong, M. Zuba, Y. Chen, N. A. Chernova, J. Bai, B. Pei, A. Goel, J. Rana, et al., *ACS Energy Lett.* **2021**, *6*, 1377–1382.
[42] K. Min, S.-W. Seo, Y. Y. Song, H. S. Lee, E. Cho, *Phys. Chem. Chem. Phys.* **2017**, *19*, 1762–1769.
[43] A. Gomez-Martin, F. Reissig, L. Frankenstein, M. Heidbüchel, M. Winter, T. Placke, R. Schmuch, *Adv. Energy Mater.* **2022**, *12*, 2103045.
[44] D. Ren, Y. Shen, Y. Yang, L. Shen, B. D. A. Levin, Y. Yu, D. A. Muller, H. D. Abruña, *ACS Appl. Mater. Interfaces* **2017**, *9*, 35811–35819.
[45] H. Z. Zhang, C. Liu, D. W. Song, L. Q. Zhang, L. J. Bie, *J. Mater. Chem. A* **2017**, *5*, 835–841.
[46] H. Arai, S. Okada, H. Ohtsuka, M. Ichimura, J. Yamaki, *Solid State Ionics* **1995**, *80*, 261–269.
[47] A. Liu, N. Phattharasupakun, R. Väli, D. Ouyang, J. R. Dahn, *J. Electrochem. Soc.* **2022**, *169*, 030538.
[48] S.-H. Lee, S. Lee, B.-S. Jin, H.-S. Kim, *Sci. Rep.* **2019**, *9*, 1–7.
[49] J. Li, N. Zhang, H. Li, A. Liu, Y. Wang, S. Yin, H. Wu, J. R. Dahn, *J. Electrochem. Soc.* **2018**, *165*, A3544–A3557.
[50] J. J. Saavedra-Arias, N. K. Karan, D. K. Pradhan, A. Kumar, S. Nieto, R. Thomas, R. S. Katiyar, *J. Power Sources* **2008**, *183*, 761–765.
[51] J. Zheng, P. Yan, L. Estevez, C. Wang, J. G. Zhang, *Nano Energy* **2018**, *49*, 538–548.
[52] X. Xiong, Z. Wang, P. Yue, H. Guo, F. Wu, J. Wang, X. Li, *J. Power Sources* **2013**, *222*, 318–325.
[53] D. D. MacNeil, Z. Lu, J. R. Dahn, *J. Electrochem. Soc.* **2002**, *149*, A1332–A1336.
[54] F. Xin, H. Zhou, X. Chen, M. Zuba, N. Chernova, G. Zhou, M. S. Whittingham, *ACS Appl. Mater. Interfaces* **2019**, *11*, 34889–34894.
[55] Y.-K. Sun, S.-T. Myung, H. J. Bang, B.-C. Park, S.-J. Park, N.-Y. Sung, *J. Electrochem. Soc.* **2007**, *154*, A937–A942.
[56] J. Li, J. Camardese, S. Glazier, J. R. Dahn, *Chem. Mater.* **2014**, *26*, 7059–7066.
[57] T. E. Conry, A. Mehta, J. Cabana, M. M. Doeff, *Chem. Mater.* **2012**, *24*, 3307–3317.
[58] M. Eilers-Rethwisch, M. Winter, F. M. Schappacher, *J. Power Sources* **2018**, *387*, 101–107.
[59] Y. Idemoto, N. Kitamura, K. Ueki, S. C. Vogel, Y. Uchimoto, *J. Electrochem. Soc.* **2012**, *159*, A673–A677.
[60] H. Zhou, F. Xin, B. Pei, M. S. Whittingham, *ACS Energy Lett.* **2019**, *4*, 1902–1906.
[61] J. Kasnatscheew, M. Evertz, B. Streipert, R. Wagner, R. Klöpsch, B. Vortmann, H. Hahn, S. Nowak, M. Amereller, A. C. Gentschev, et al., *Phys. Chem. Chem. Phys.* **2016**, *18*, 3956–3965.
[62] R. Weber, C. R. Fell, J. R. Dahn, S. Hy, *J. Electrochem. Soc.* **2017**, *164*, A2992–A2999.
[63] S.-U. Woo, C. S. Yoon, K. Amine, I. Belharouak, Y.-K. Sun, *J. Electrochem. Soc.* **2007**, *154*, A1005–A1009.
[64] X. Song, G. Liu, H. Yue, L. Luo, S. Yang, Y. Huang, C. Wang, *Chem. Eng. J.* **2021**, *407*, 126301.
[65] Y. Su, Q. Zhang, L. Chen, L. Bao, Y. Lu, Q. Shi, J. Wang, S. Chen, F. Wu, *ACS Appl. Mater. Interfaces* **2020**, *12*, 37208–37217.
[66] H. Lu, H. Zhou, A. M. Svensson, A. Fossdal, E. Sheridan, S. Lu, F. Vullum-Bruer, *Solid State Ionics* **2013**, *249–250*, 105–111.
[67] F. Wu, Q. Li, L. Chen, Q. Zhang, Z. Wang, Y. Lu, L. Bao, S. Chen, Y. Su, *ACS Appl. Mater. Interfaces* **2019**, *11*, 36751–36762.
[68] Y. Jiang, Y. Bi, M. Liu, Z. Peng, L. Huai, P. Dong, J. Duan, Z. Chen, X. Li, D. Wang, et al., *Electrochim. Acta* **2018**, *268*, 41–48.
[69] Y. Bi, W. Yang, R. Du, J. Zhou, M. Liu, Y. Liu, D. Wang, *J. Power Sources* **2015**, *283*, 211–218.
[70] E. Björklund, D. Brandell, M. Hahlin, K. Edström, R. Younesi, *J. Electrochem. Soc.* **2017**, *164*, A3054–A3059.
[71] P. Teichert, H. Jahnke, E. Figgemeier, *J. Electrochem. Soc.* **2021**, *168*, 090532.
[72] H. Li, A. Liu, N. Zhang, Y. Wang, S. Yin, H. Wu, J. R. Dahn, *Chem. Mater.* **2019**, *31*, 7574–7583.
[73] K.-J. Park, J.-Y. Hwang, H.-H. Ryu, F. Maglia, S.-J. Kim, P. Lamp, C. S. Yoon, Y. K. Sun, *ACS Energy Lett.* **2019**, *4*, 1394–1400.
[74] C. S. Yoon, H.-H. Ryu, G.-T. Park, J.-H. Kim, K.-H. Kim, Y.-K. Sun, *J. Mater. Chem. A* **2018**, *6*, 4126–4132.
[75] T. Weigel, F. Schipper, E. M. Erickson, F. A. Susai, B. Markovsky, D. Aurbach, *ACS Energy Lett.* **2019**, *4*, 508–516.
[76] F. Wu, J. Tian, Y. Su, J. Wang, C. Zhang, L. Bao, T. He, J. Li, S. Chen, *ACS Appl. Mater. Interfaces* **2015**, *7*, 7702–7708.
[77] X. Zheng, X. Li, B. Zhang, Z. Wang, H. Guo, Z. Huang, G. Yan, D. Wang, Y. Xu, *Ceram. Int.* **2016**, *42*, 644–649.
[78] S. U. Woo, B.-C. Park, C. S. Yoon, S.-T. Myung, J. Prakash, Y.-K. Sun, *J. Electrochem. Soc.* **2007**, *154*, A649–A655.
[79] R. Weber, A. J. Louli, K. P. Plucknett, J. R. Dahn, *J. Electrochem. Soc.* **2019**, *166*, A1779–A1784.
[80] H. Brandstätter, I. Hanzu, M. Wilkening, *Electrochim. Acta* **2016**, *207*, 218–223.
[81] D. A. Harrington, B. E. Conway, *Electrochim. Acta* **1987**, *32*, 1703–1712.

Manuscript received: August 12, 2022
Revised manuscript received: September 2, 2022
Accepted manuscript online: September 5, 2022